IEEE Access
Multidisciplinary ⋮ Rapid Review ⋮ Open Access Journal

Received January 30, 2022, accepted February 28, 2022, date of publication March 2, 2022, date of current version March 10, 2022.

Digital Object Identifier 10.1109/ACCESS.2022.3156294

Analytical Study of Dirac Type Dispersion in Simple Periodic Waveguide Structures for Leaky-Wave Applications

SINA REZAEE[1], MOHAMMAD MEMARIAN[1], (Senior Member, IEEE), AND GEORGE V. ELEFTHERIADES[2], (Fellow, IEEE)

[1]Department of Electrical Engineering, Sharif University of Technology, Tehran 14588-89694, Iran
[2]The Edward S. Rogers Sr. Department of Electrical and Computer Engineering, University of Toronto, Toronto, ON M5S 2E4, Canada

Corresponding author: Mohammad Memarian (mmemarian@sharif.edu)

ABSTRACT In this work, we present a study on the existence of Dirac type dispersion in the simplest of periodic metallic waveguide structures. It is shown that periodic repetitions of two dissimilar waveguides (WGs) can be properly designed to lead to a Dirac type dispersion. A simple theory using circuit modeling is presented to find the condition for Dirac point operation. In addition, mode-matching followed by full-wave simulations validate that the band structure matches that of the theory and shows that a Dirac dispersion can be realized. A Dirac Leaky-Wave Antenna (DLWA) is then implemented using this simple arrangement in substrate-integrated-waveguide (SIW) technology. This DLWA has the closed broadside stopband feature, leading to continuous frequency beam scanning through broadside and a simple feeding network. Phase and leakage constants are adjusted to yield a directive fan-beam featuring continuous scanning in a wide range of angles. The presented DLWA has a wide impedance bandwidth with high efficiency and operates with peak gains of about 12.5 dBi without any significant gain variation throughout the frequency range from 13.5 GHz to 16.5 GHz. Measured results show excellent agreement with the simulated results, validating the proposed concepts.

INDEX TERMS Dirac leaky-wave antenna, mode-matching technique, broadside radiation, frequency scanning antenna, substrate integrated waveguide (SIW), microwave applications.

I. INTRODUCTION

Many fascinating transport properties, such as the quantum Hall effect, the Zitterbewegung, and the Klein paradox, are enabled by Dirac-type cones in the dispersion band of electron systems, which provide a linear relationship between the electron energy and the wave number at the corner of the Brillouin zone, as in the electric band of graphene near the Fermi level [1]. Two-dimensional (2D) photonic crystals (PCs) have also been shown to exhibit conical Dirac dispersion diagrams at their band center in the past decade, spurring significant research interest since their discovery [2]. This observation led to PCs with zero effective refractive index and thus the interesting and useful properties, and features of such media were made available [3]. Aside from this wave transport property, the Dirac cone dispersion was later shown to provide a means to engineer new antennas without any bandgap, the so-called Dirac Leaky- Wave Antenna (DLWA) [4]–[7].

Leaky-Wave Antennas (LWAs) date back to the 1940s, where Hansen proposed the first of such antenna consisting of a metallic waveguide loaded with a radiating long slot along its sidewall [8]. Since then, LWAs have been widely studied and applied for various applications such as communication systems [6], automotive radar and high-resolution sensor applications [9], weather radars [10], etc. due to their attractive characteristics such as high directive beams, frequency-scanned beams, and a simple feeding network. Periodic structures can be made to have a space harmonic in the fast region, making them a traveling-wave structure that leaks power gradually along its length [5]. Periodic LWAs are advantageously able to scan both backward and forward beams w.r.t broadside, but due to the coupling of Bloch modes, they typically suffer from the problem of open-stopband at broadside (leading to lack of radiation at broadside and fluctuation in gain and efficiency while

The associate editor coordinating the review of this manuscript and approving it for publication was Raghvendra Kumar Kumar Chaudhary.

scanning) [7]. The existence of a stopband at broadside in periodic LWAs is due to the contra-directional coupling of two radiating Floquet harmonics as described in [18], [28].

The open stop-band issue could be addressed as in [11] with metamaterial-inspired Composite Right-Left Handed (CRLH) LWAs, where the antenna is only radiating through the n=0 harmonic. Several types of CRLH/metamaterial-based LWAs have been proposed in [19]–[22]. In [22], a mm-wave band LWA based on half mode SIW technology incorporating CRLH media is proposed. The LWA utilizes interdigital capacitive slots to improve sidelobe level (SLL) and achieve higher gain. Also, double-strip grating LWAs with broadside scan [23] have been presented thus far. In another approach, the Dirac leaky-wave antenna (DLWA) for continuous beam scanning from photonic crystals was reported in [5]. Unlike the small unit-cell of metamaterials ($\ll \lambda_g$), DLWAs have larger unit-cells and, in turn, reduced complexity and ease of fabrication, especially at higher frequencies. In the first DLWA work [5], it was demonstrated that an interface of a Dirac PC (DPC) can be made to radiate in a leaky-wave fashion, enabling a one-dimensional (1D) DLWA for the terahertz frequency band. But this DLWA proposal would require two types of dielectrics embedded within each other. This problem was solved with a notable simplification in [6], [7], showing that the DLWA may be implemented in Substrate Integrated Waveguide (SIW) technology for the millimeter-wave band. Furthermore, due to a closed band gap at the center of the Brillouin zone of 2D DPCs, a 2D DLWA with circular polarization radiation and excellent axial ratio was shown in [12]. Also, due to similarities between the unit cell of Transmission-Line (TL) grids and DPCs, 2D DLWAs were presented in [13]–[15]. A method has been presented to open stopband suppression in LWAs based on a Varied Uniform Guided-Wave Structure (VUGS) and studied analytically at microwave frequencies [16]. The most recent Ridge Gap Waveguide (RGW) based DLWA is presented in [17], which comprises alternated silicon rods for terahertz applications and its equivalent circuit is provided which verifies the proper closure of the bandgap. This LWA shows interesting characteristics such as a high gain fan-beam exactly at broadside, wide frequency-based beam steering, and low cross-polarization. Also, in [18] a new approach is presented to generate a scannable pencil beam using an extended parallel-plate-based Dirac PC. In all work presented thus far on DLWAs, even those with SIW, structures require some forms of through or semi-covered holes to achieve all the requirements. This complicated the analysis to yield a simple equivalent circuit model to prove and find the conditions for the Dirac conditions and the closed-stopband.

In this paper, we first aim to show how the Dirac dispersion is indeed possible in the simplest of periodic waveguide structures, using simple equivalent circuits and Bloch analysis. We then utilize a related structure to analyze and design for Dirac operation. This structure is then realized in SIW technology to lead to a Dirac LWA with exceptional performance. The design presented here is much simpler than that of [5]–[7] and [16], [17], as it is easier to design and fabricate, and has exceptional performance.

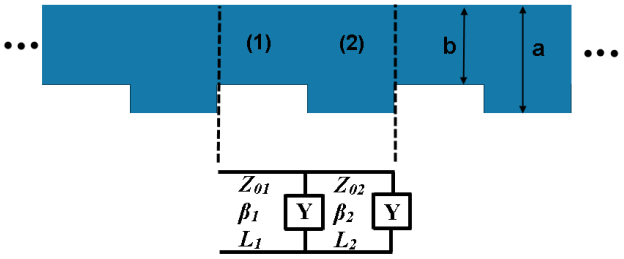

FIGURE 1. The geometry and equivalent circuit model of the considered unit cell.

II. DIRAC DISPERSION CONDITION

Consider Fig. 1 showing a simple periodic air-filled waveguiding structure with the constituent unit cell comprising two cascaded waveguides (WGs) with different widths a and b.

To find the dispersion relation of all the Floquet-Bloch modes in the structure, we first note the equivalent circuit and the ABCD parameters of the unit cell. The single-mode waveguide sections can be modelled as transmission lines and the step discontinuity due to width change as a shunt admittance (inductance) [24]. Therefore, the ABCD parameters of one unit cell are

$$\begin{bmatrix} A_U(\omega) & B_U(\omega) \\ C_U(\omega) & D_U(\omega) \end{bmatrix} = ABCD_1(\omega) \times \begin{bmatrix} 1 & 0 \\ Y & 1 \end{bmatrix} \times ABCD_2(\omega) \times \begin{bmatrix} 1 & 0 \\ Y & 1 \end{bmatrix} \quad (1a)$$

where

$$ABCD_i = \begin{bmatrix} \cos(\beta_i L_i) & jZ_{0i}\sin(\beta_i L_i) \\ \frac{j}{Z_{0i}}\sin(\beta_i L_i) & \cos(\beta_i L_i) \end{bmatrix}$$
$$\beta_i = \sqrt{\omega^2\mu\varepsilon - \left(\frac{\pi}{w_i}\right)^2}$$
$$Y = \frac{1}{j\omega L} \quad (1b)$$

In (1), Z_{0i}, γ_i, L_i and w_i are the characteristic impedance, propagation constant, length and width of the waveguide sections, respectively, where $i = 1$ or 2. The amount of shunt admittance used in Y is typically modelled based on the discontinuity of the WGs as [24]:

$$L = -\frac{Z_{01}(1+A)}{\omega(1-A)} \quad (2a)$$

where

$$A = \frac{\frac{4Z_{02}I^2}{ab} - Z_{01}}{\frac{4Z_{02}I^2}{ab} + Z_{01}}$$
$$I = \int_{x=0}^{b} \sin(\frac{\pi x}{a})\sin(\frac{\pi x}{b})dx \quad (2b)$$

The Bloch phase constant (β_B) of a propagating Bloch mode can now be written as

$$\beta_B = \frac{\cos^{-1}((A_U(\omega) + D_U(\omega))/2)}{p} \tag{3a}$$

where p is the period of the structure ($p = L_1 + L_2$) and for our unit-cell equivalent circuit:

$$\begin{aligned}\frac{A_U(\omega) + D_U(\omega)}{2} &= \frac{1}{4}\left(2 + \frac{Z_{01}}{Z_{02}} + \frac{Z_{02}}{Z_{01}} - \frac{Z_{01}Z_{02}}{\omega^2 L^2}\right)\cos(\beta_1 L_1 + \beta_2 L_2) \\ &+ \frac{1}{4}\left(2 - \frac{Z_{01}}{Z_{02}} - \frac{Z_{02}}{Z_{01}} + \frac{Z_{01}Z_{02}}{\omega^2 L^2}\right)\cos(\beta_1 L_1 - \beta_2 L_2) \\ &+ \frac{(Z_{01} + Z_{02})}{2\omega L}\sin(\beta_1 L_1 + \beta_2 L_2) \\ &+ \frac{(Z_{01} - Z_{02})}{2\omega L}\sin(\beta_1 L_1 - \beta_2 L_2)\end{aligned} \tag{3b}$$

Eq (3) is the dispersion relation governing the periodic structure. For the Dirac condition to occur, we essentially seek that a solution exists everywhere at and around $\beta_B = 0$ at a particular design frequency f_D (and with a linear dispersion), such that no stopband is formed. In other words, in (3b), (A+D)/2 would always be smaller or equal to 1 and never above 1. Due to the local maxima behavior of (A+D)/2, in order for the bandgap to close i.e. Dirac point to occur, (A+D)/2 would be equal to 1 and its derivative equal to 0 only at the Dirac frequency. Thus, at the Dirac point

$$\begin{aligned}\frac{A_U(\omega) + D_U(\omega)}{2} &= 1 \\ \frac{d}{d\omega}\left(\frac{A_U(\omega) + D_U(\omega)}{2}\right) &= 0\end{aligned} \tag{4}$$

There are many solutions to this problem depending on choice of f_D and unit-cell size, and the WG widths chosen. For simplicity, let us choose $\beta_2 L_2 = \pi$, (3b) is thus simplified as:

$$\frac{A_U(\omega) + D_U(\omega)}{2} = \frac{-Z_{01}}{\omega L}\sin(\beta_1 L_1) - \cos(\beta_1 L_1) \tag{5}$$

thus, to find L_1, two following transcendental equation should simultaneously be solved, which are obtained from using (5) in (4).

$$\begin{aligned}&\frac{-Z_{01}}{\omega L}\sin(\beta_1 L_1) - \cos(\beta_1 L_1) = 1 \\ &\times \frac{Z_{01}\beta_1 + \omega^2 \mu\varepsilon L L_1}{\omega^2 L \beta_1}\sin(\beta_1 L_1) - \frac{Z_{01}\omega\mu\varepsilon L_1}{\omega L \beta_1} \\ &\times \cos(\beta_1 L_1) = 0\end{aligned} \tag{6}$$

leading to the design of L_2 to achieve the Dirac dispersion in a simple two WG unit-cell, with the discontinuities accounted for.

The dispersion diagram for the particular design dimensions (a = 13 mm, b = 12mm, L_2 = 18.05mm, L_1 = 16.65mm) of the Fig. 1 structure is shown in Fig. 2. As can be seen, a closed bandgap is obtained in the analytical results

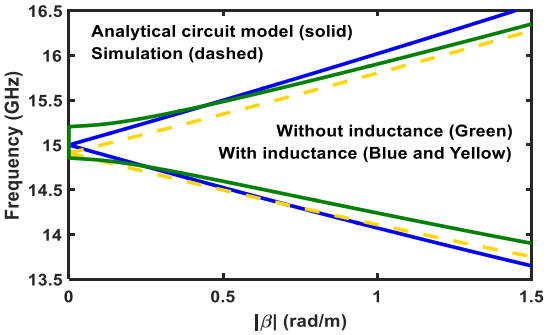

FIGURE 2. The dispersion diagram of the unit cell (FIGURE 1) is obtained from the presented formulations and simulation for the particular design dimensions (a=13mm, b=12mm, L_2 = 18.05mm, L_1 = 16.65mm).

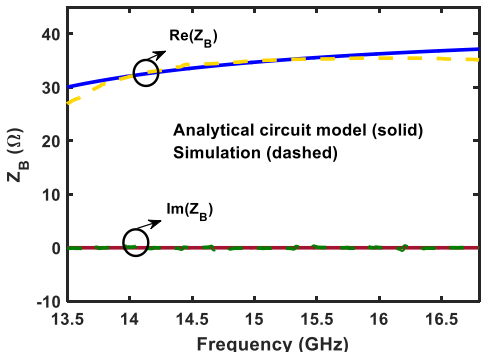

FIGURE 3. The Bloch impedance of the unit cell (FIGURE 1) is obtained from the presented formulations and simulation.

(Blue curve) at $|\beta_B| = 0$, when the inductances were considered in the model and lengths were designed for using (6). Also, full-wave simulation results show a closed bandgap with just a small shift in Dirac frequency point (yellow curve). The small shift between circuit and full-wave results mainly stems from the modelling of the discontinuities with a shunt inductor, which has its limitations. However, if the inductance values were not considered in the dispersion calculation process, not only a higher shifting in operation frequency point would be experienced, but also a large bandgap would be opened (green curve).

The Bloch impedance of the model can now be written as

$$Z_B = \frac{-2B_U(\omega)}{A_U(\omega) - D_U(\omega) \pm \sqrt{((A_U(\omega) + D_U(\omega))^2 - 4}} \tag{7}$$

The Bloch impedance for the particular design dimensions of Fig. 1 structure leading to an almost completely real impedance is shown in Fig. 3. Although the simulated results for Bloch impedance are obtained from driven-mode simulation of the finite unit cells, a good agreement can be seen between the analytical circuit model and full-wave simulation results. In the following, non-shielded structures that experience radiation loss within the unit cell are discussed in the next sections.

III. THE 1D DIRAC PC

A difficulty in reusing the design of [5] was the need for two types of dielectrics embedded within each other, needing

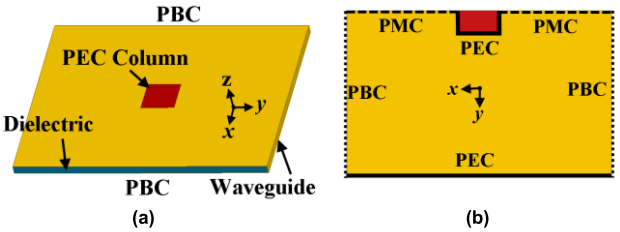

FIGURE 4. (a) The geometry of proposed 1D Dirac PC. (b) Simplified unit cell utilizing the transversal symmetry.

special fabrication, rendering it unusable for standard planar fabrication. Also, limited accuracy of air through-hole fabrication and the need for a back plate in [6] leads to differences in the results than the ideal design due to tolerances, let alone preventing their exact analysis with simple circuit models. In order to avoid these difficulties, we use the simple PC discussed herein which would be ideal for 3D and planar fabrication, e.g. with SIW technology. Using the results of the previous section showing how Dirac Dispersion can be realized in the simplest of WG structures, we embark on proposing a unit-cell and analyze it using an accurate mode-matching technique to verify the simulation results.

Fig. 4(a) shows the geometry of the proposed 1D DPC. As shown, we use a metallic square column inside a host dielectric-filled metallic waveguide. The metallic column is placed at the center of the unit cell with a square cross-section. As will be shown, with the periodic repetition of this cell, two Bloch modes will arise that can be made degenerate at the broadside frequency in order to achieve both frequency and Q balancing, for continuous beam scanning. This concept of forced accidental degeneracy of eigenmodes was used in dielectric resonators [25], and later used in [5] for DPCs. To avoid multiple full wave eigenmode simulations, the analytical approach leads to the dispersion diagram, expediting the design process.

The problem under study is to compute the dispersion diagram for the unit cell shown in Fig. 4(a). The unit cell is completely symmetrical in the transversal direction and the metallic waveguide is idealized with Perfect Electric Conductor (PEC) walls. For the ease in analysis, an auxiliary unit cell is introduced in Fig. 4(b). Due to transversal symmetry of the unit cell, only half of the original unit cell is studied and the middle boundary is considered a Perfect Magnetic Conductor (PMC). Computing scattering parameters of the unit cell are necessary for obtaining the dispersion diagram.

A. MODE-MATCHING FORMULATIONS FOR DISCONTINUITY

For the analysis of the step discontinuity, the mode-matching technique is used and the longitudinal PEC wall at the discontinuity is recessed to create a new region C (Fig. 5). The original unit cell is recovered when $d = 0$. It can be assumed the electric field is constant in the z-direction as long as planar technology is used. The mode-matching process starts by

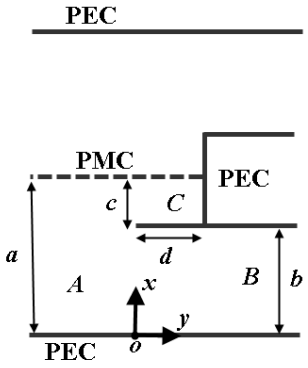

FIGURE 5. Auxiliary geometry of step discontinuity.

expanding the tangential electric and magnetic fields for TE_{n0} ($n = 0, 1, \ldots$) modes on both sides of the junction. The E_z continuity equation reads

$$\sum_{n=0}^{M-1}(A_n^+ + A_n^-)\varphi_{an} = \begin{cases} \sum_{n=0}^{K-1}(B_n^+ + B_n^-)\varphi_{bn}, & 0 \le x \le b \\ \sum_{n=0}^{L-1} C_n\varphi_{cn}(1+\rho_n), & b \le x \le a \end{cases} \tag{8a}$$

and for H_x

$$\sum_{n=0}^{M-1}(A_n^+ - A_n^-)Y_{an}\varphi_{an} = \begin{cases} \sum_{n=0}^{K-1}(B_n^+ - B_n^-)Y_{bn}\varphi_{bn}, & 0 \le x \le b \\ \sum_{n=0}^{L-1} C_n Y_{cn}\varphi_{cn}(1-\rho_n), & b \le x \le a \end{cases} \tag{8b}$$

where

$$\varphi_{an} = \sqrt{\frac{2}{a}}\sin(k_a x), \quad k_a = \frac{(2n+1)\pi}{2a}, \quad Y_{an} = \sqrt{k^2 - k_a^2}$$
$$\varphi_{bn} = \sqrt{\frac{2}{b}}\sin(k_b x), \quad k_b = \frac{(n+1)\pi}{b}, \quad Y_{bn} = \sqrt{k^2 - k_b^2}$$
$$\varphi_{cn} = \sqrt{\frac{2}{c}}\cos((a-x)k_c), \quad k_c = \frac{(2n+1)\pi}{2c},$$
$$Y_{cn} = \sqrt{k^2 - k_c^2}$$
$$\rho_n = e^{2jY_{cn}d}$$

In (9), φ_{an}, φ_{bn} and φ_{cn} are normal modes in Regions A, B, and C, with propagation constants Y_{an}, Y_{bn}, and Y_{cn}, respectively. Region B has a different expression for the wavenumber than in regions A and C, as region B has PEC on both sidewalls. A_{n}^+, A_{n}^- and B_{n}^+, B_{n}^- and C_{n}^+, C_{n}^- are the field coefficients in regions A, B, and C, respectively. ρn is the reflection from the PEC wall in Region C. From modal

orthogonality, we obtain the linear synchronous equations modal coefficients.

$$
\begin{aligned}
&A_m^+ + A_m^- \\
&\quad = \sum_{n=1}^{K} H_{mn}(B_n^+ + B_n^-) + \sum_{n=1}^{L} \overline{H}_{mn} C_n (1+\rho_n) \\
&Y_{am}(A_m^+ - A_m^-) \\
&\quad = \sum_{n=1}^{K} H_{mn} Y_{bn}(B_n^+ - B_n^-) + \sum_{n=1}^{L} \overline{H}_{mn} Y_{cn} C_n (1-\rho_n) \\
&\qquad m = 0, 1, ..M-1 \qquad (9a) \\
&\sum_{n=0}^{M-1} H_{nm}(A_n^+ + A_n^-) \\
&\quad = B_m^+ + B_m^- \\
&\sum_{n=0}^{M-1} H_{nm} Y_{an}(A_n^+ - A_n^-) \\
&\quad = Y_{bn}(B_m^+ - B_m^-) \quad m = 0, 1, ..K-1 \qquad (9b) \\
&\sum_{n=0}^{M-1} \overline{H}_{nm}(A_n^+ + A_n^-) \\
&\quad = C_m(1+\rho_m) \\
&\sum_{n=0}^{M-1} \overline{H}_{nm} Y_{an}(A_n^+ - A_n^-) \\
&\quad = C_m Y_{cm}(1-\rho_m) \quad m = 0, 1, ..L-1 \qquad (9c)
\end{aligned}
$$

where

$$
\begin{aligned}
H_{mn} &= \int_0^b \varphi_{am}\varphi_{bn} dx = \frac{2k_{bn}(-1)^{n+1}\sin(k_{am}b)}{\sqrt{ab}(k_{am}^2 - k_{bn}^2)} \\
\overline{H}_{mn} &= \int_b^a \varphi_{am}\varphi_{cn} dx = \frac{2k_{cn}(-1)^{n+1}\sin(k_{am}b)}{\sqrt{ac}(k_{am}^2 - k_{cn}^2)} \qquad (10)
\end{aligned}
$$

The following matrices are used to compress the aforementioned equations:

$$
\begin{aligned}
Y_i &= \begin{bmatrix} Y_{i1} & 0 & \cdots & \\ 0 & Y_{i2} & & \\ \vdots & & \ddots & \\ & & & Y_{in} \end{bmatrix} \\
&\quad n = M, K, L \\
&\quad i = a, b, c \\
R &= \begin{bmatrix} 1+\rho_1 & 0 & \cdots & \\ 0 & 1+\rho_2 & & \\ \vdots & & \ddots & \\ & & & 1+\rho_n \end{bmatrix}, \\
R' &= \begin{bmatrix} 1-\rho_1 & 0 & \cdots & \\ 0 & 1-\rho_2 & & \\ \vdots & & \ddots & \\ & & & 1-\rho_n \end{bmatrix}
\end{aligned}
$$

$$
\begin{aligned}
&n = L-1 \\
Y_d &= \begin{bmatrix} Y_b & 0 \\ 0 & Y_c \end{bmatrix}, \quad \overline{R'} = \begin{bmatrix} I & 0 \\ 0 & R' \end{bmatrix}, \overline{R} = \begin{bmatrix} I & 0 \\ 0 & R \end{bmatrix}, \\
G &= \begin{bmatrix} H & \overline{H} \end{bmatrix}
\end{aligned}
$$

where I is the identity matrix, H is a matrix of size $M \times K$ with generic element, H_{mn} as defined above, while $\overline{H}$ is a matrix of size $M \times L$ with generic element $\overline{H}_{mn}$. The mode-matching equations may therefore be represented in matrix form as follows:

$$
\begin{aligned}
a^+ + a^- &= G\overline{R}d^+ + Gd^- && (11a) \\
Y_a(a^+ - a^-) &= GY_d\overline{R}'d^+ - GY_d d^- && (11b) \\
G^T(a^+ + a^-) &= \overline{R}d^+ + d^- && (11c) \\
G^T Y_a(a^+ - a^-) &= Y_d\overline{R}'d^+ - d^- && (11d)
\end{aligned}
$$

where superscript ^{T} denotes the transpose operation. a^+ and b^- are column vectors of the excitation coefficients and a^- and b^+ are column vectors of the unknown modal coefficients:

$$
a^+ = \begin{bmatrix} A_1^+ \\ A_2^+ \\ \vdots \\ A_M^+ \end{bmatrix}_{M\times 1}, \quad d^- = \begin{bmatrix} B_1^- \\ B_2^- \\ \vdots \\ B_K^- \\ 0 \\ \vdots \\ 0 \end{bmatrix}_{M\times 1},
$$

$$
a^- = \begin{bmatrix} A_1^- \\ A_2^- \\ \vdots \\ A_M^- \end{bmatrix}_{M\times 1}, \quad d^+ = \begin{bmatrix} B_1^+ \\ B_2^+ \\ \vdots \\ B_K^+ \\ 0 \\ \vdots \\ 0 \end{bmatrix}_{M\times 1}
$$

The unknown field coefficients are obtained from the simultaneous solution of the above equations. After solving these equations and calculating the unknown coefficients, the S-parameters and then the transfer matrix of the step discontinuity can be obtained as follows:

$$
\begin{aligned}
S_{11} &= \frac{A_1^-}{A_1^+}, \quad S_{21} = \frac{B_1^-}{A_1^+}, \; S_{22} = \frac{B_1^-}{B_1^+}, \; S_{12} = \frac{A_1^-}{B_1^+} \qquad (12) \\
A &= \frac{(1+S_{11})(1-S_{22}) + S_{12}S_{21}}{2S_{21}}, \\
B &= Z_0 \frac{(1+S_{11})(1+S_{22}) - S_{12}S_{21}}{2S_{21}} \\
C &= \frac{1}{Z_0} \frac{(1-S_{11})(1-S_{22}) - S_{12}S_{21}}{2S_{21}}, \\
D &= \frac{(1-S_{11})(1+S_{22}) + S_{12}S_{21}}{2S_{21}} \qquad (13)
\end{aligned}
$$

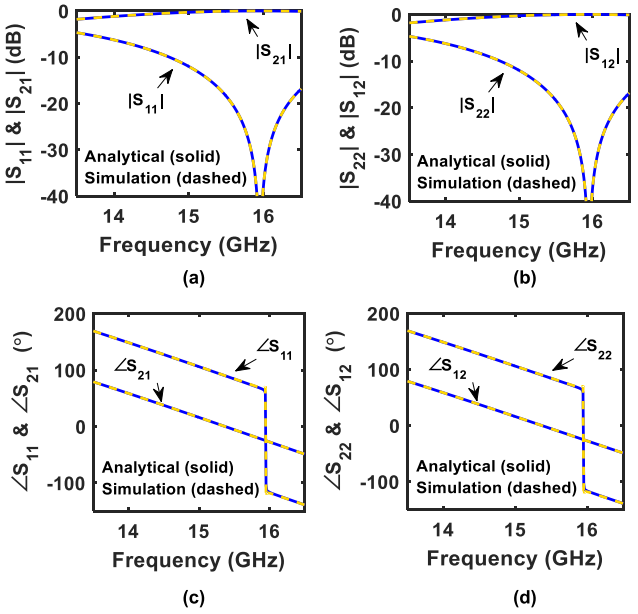

FIGURE 6. The comparison between the S-parameters of the auxiliary unit cell (Fig. 3(b)) is obtained from the analysis and the driven-mode simulation results of the original unit cell (Fig. 3(a)). (a) Magnitude of S_{11} and S_{21}. (b) Magnitude of S_{22} and S_{12}. (c) Phase of S_{11} and S_{21}. (d) Phase of S_{22} and S_{12}.

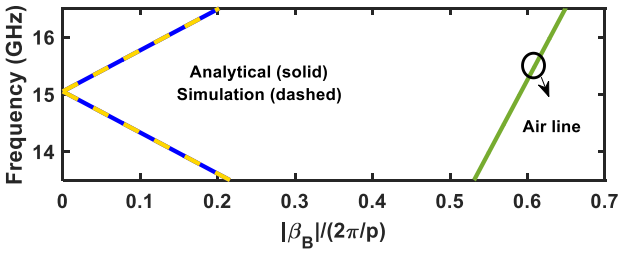

FIGURE 7. The comparison between the dispersion diagrams of the unit cell is obtained from the analytical process and the driven-mode simulation.

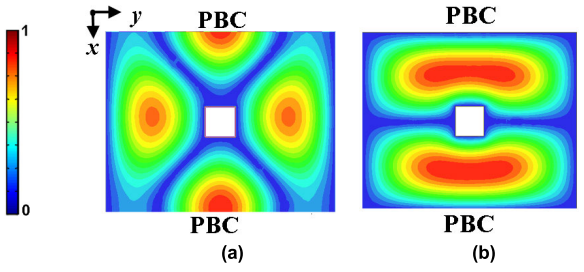

FIGURE 8. (a-b) Normalized intensity of E-field magnitude of symmetry (even mode) and asymmetry (odd mode) Bloch eigenmodes for the one dimensional Dirac PC, respectively.

B. TRANSFER MATRIX COMBINATION FOR UNIT CELL S-PARAMETERS CALCULATION

By dividing the unit cell into several sections and combining their transfer matrices, the transfer matrix of the unit cell is written as

$$[ABCD_{Total}] = \begin{bmatrix} ABCD_1 \\ Transmission\ Line(L_1) \end{bmatrix} \times \begin{bmatrix} ABCD_2 \\ Discontinuity \end{bmatrix} \times \begin{bmatrix} ABCD_3 \\ Transmission\ Line(L_2) \end{bmatrix} \times \begin{bmatrix} ABCD_4 \\ Discontinuity \end{bmatrix} \times \begin{bmatrix} ABCD_1 \\ Transmission\ Line(L_1) \end{bmatrix} \quad (14a)$$

The transfer matrix of the first step discontinuity ($ABCD_2$) is computed from the results of the previous section. The other transfer matrices are computed in the following form.

$$ABCD_1 = \begin{bmatrix} \cosh(-jY_{a1}L_1) & Z_{01}\sinh(-jY_{a1}L_1) \\ Y_{01}\sinh(-jY_{a1}L_1) & \cosh(-jY_{a1}L_1) \end{bmatrix}$$
$$ABCD_3 = \begin{bmatrix} \cosh(-jY_{b1}L_2) & Z_{02}\sinh(-jY_{b1}L_2) \\ Y_{02}\sinh(-jY_{b1}L_2) & \cosh(-jY_{b1}L_2) \end{bmatrix}$$
$$ABCD_2 = \begin{bmatrix} A_2 & B_2 \\ C_2 & D_2 \end{bmatrix} \quad ABCD_4 = \begin{bmatrix} D_2 & B_2 \\ C_2 & A_2 \end{bmatrix} \quad (14b)$$

The S-parameters comparisons between the simulation of the original unit cell (Fig. 4(a)) using Ansys HFSS and analysis results of the auxiliary unit cell (Fig. 4(b)) are shown in Fig. 6, confirming the validity of the analysis. In the last step, the dispersion diagram is obtained from (2b) which is presented in Fig.7. As can be seen, Dirac dispersion is achieved for the desired operation frequency of 15.05 GHz with particular dimensions and the analysis results are in excellent agrrement with the simulated results.

Eigenmode simulations of the periodic cell at the band center shows that two orthogonal modes have arisen that are degenerate at the Dirac frequency (f_D = 15GHz), leading to a 1D Dirac-type dispersion for the DPC. The normalized intensities of the electric field magnitude of two Bloch eigenmodes at the Γ-point are shown in Fig. 7. The field pattern that is shown in Fig. 8(a) has symmetry relative to the unit cell center (even mode) therefore has no radiation in the broadside direction. But the field pattern shown in Fig. 8(b)

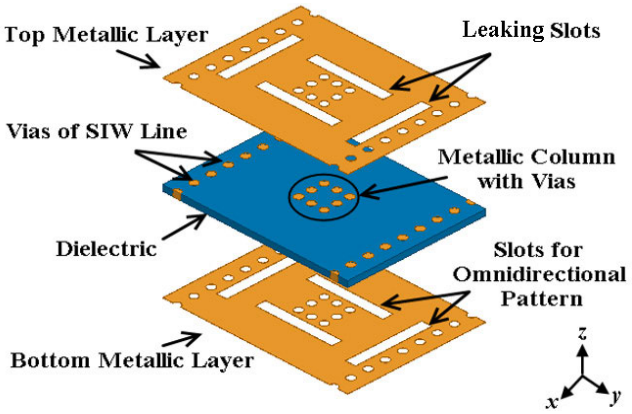

FIGURE 9. The geometry of the proposed 1D leaky Dirac PC.

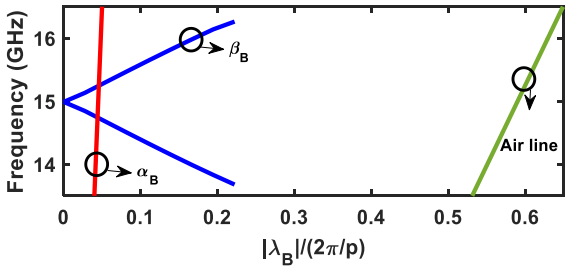

FIGURE 10. Dispersion diagram and the attenuation constant of the proposed 1D leaky Dirac PC.

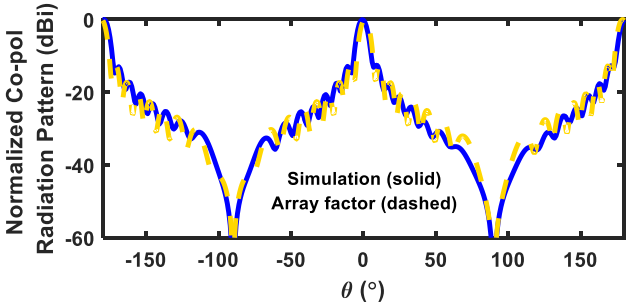

FIGURE 11. The comparison between normalized radiation patterns obtain from simulation and theoretical approximation based on the array factor approach.

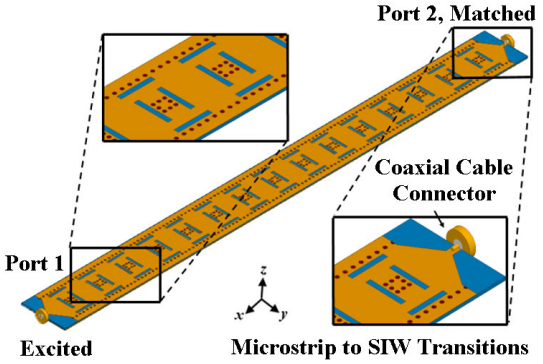

FIGURE 12. The proposed DLWA. (a) The 3D view of the geometry of the proposed DLWA. (b) Photograph of the manufactured prototypes.

has asymmetry in the x-direction (odd mode) and provides far-field broadside radiation.

IV. THE LEAKY 1D DIRAC PC

For the implementation of the proposed DPC, we utilize SIW technology for realizing the PEC walls (the difference between the effective width of the PEC wall and the SIW implementation is considered). Fig. 9 shows the geometry of the proposed 1D leaky DPC. In order to leak out electromagnetic energy from the Bloch eigenmodes, two types of slots (transversal and longitudinal for the odd and even eigenmode, respectively) are made on the top and bottom layers. This form of slot arrangement is suitable for realizing an omnidirectional radiation pattern. The size of the slots is designed so that Q-balancing ($Q_{\text{even}} = Q_{\text{odd}}$) is achieved. But inserting the slots ultimately opens a stopband again. In order to fix this problem, the dimensions are adjusted again in an eigenmode solver. Fig. 10 shows the dispersion diagram of the proposed 1D leaky Dirac PC. As it can be seen, the closed stop-band occurs at $|\beta_B| = 0$, and Dirac dispersion is attained.

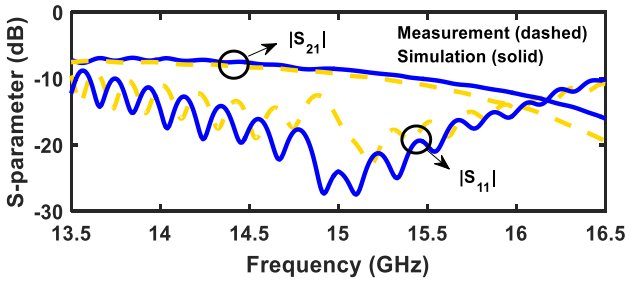

FIGURE 13. The simulated and measured scattering parameter of the DLWAs.

For radiation pattern estimation, the array factor approach was applied. As previously mentioned, the even mode has no far-field radiation in the broadside direction. Therefore, only the odd mode is considered for radiation pattern calculation. The odd mode radiates from both the transversal slots.

Because of the phase difference between the slots (from the nature of the odd mode), far-field radiations are augmented with each other. Each slot operates similar to a small magnetic dipole, radiating in space. Therefore, the radiation pattern of each unit cell will approximately be $RU(\theta) = \sin(\theta + \pi/2)$. Based on the array factor approach of 1D LWAs as in [26], a LWA can be considered as a phased array antenna with inter-element spacing p. The LWA is excited continuously with a discretized phase function (φ_n), a discretized exponential magnitude function (I_n), and the radiation angle (θ_0).

$$\begin{aligned} \varphi_n &= -(n-1)k_0 p \sin\theta_0 \\ I_n &= I_0 e^{-\alpha(n-1)p} \\ \theta_0 &= \sin^{-1}\left[\left(\beta(\omega) + 2\pi q/p\right)/k_0\right] \end{aligned} \tag{15a}$$

where α is the leakage factor, p is the period of the LWA, k_0 is the free space wavenumber, $\beta(\omega)$ is the propagation constant in the direction of propagation and q is an integer indicating the space harmonic index. In this regard, the final co-pol. radiation pattern can be well estimated by $R(\theta)$.

$$R(\theta) = R_U(\theta) \times AF(\theta)$$

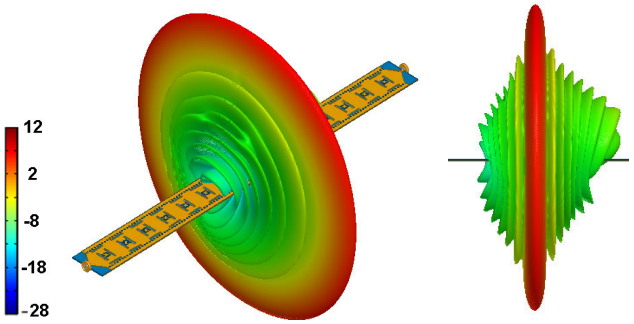

FIGURE 14. Three-dimensional radiation pattern of the 15-cell DLWA (in a 40-dB scale range), showing an omnidirectional narrow fan beam pointing right at broadside.

$$= \sin(\theta + \frac{\pi}{2}) \times \sum_{n=1}^{N} I_n e^{j(n-1)k_0 p \sin\theta + j\varphi_n} \qquad (15b)$$

where N represents the number of unit cells comprising the LWA. Fig. 11 shows the normalized co-pol. radiation pattern obtained by (16) with $N = 15$. Excellent agreement can be seen between simulation and theoretical approximation based on the array factor approach.

V. DIRAC LEAKY-WAVE ANTENNA (DLWA)

The complete SIW DLWA is made directly from cascading the unit cells described previously. The geometry of the DLWA is shown in Fig. 12(a). The number of the unit cells ($N = 15$) is chosen to be long enough to radiate most of the incident power. The microstrip to SIW transitions are designed to impedance match between the microstrip mode ($Z_0 = 50\Omega$) and the Bloch mode of the DLWA ($Z_B \approx 4\Omega$), over a wide bandwidth. The transition's primary dimensions were estimated using [27], and final values were achieved by fine-tuning the structure using a full-wave solver. The geometrical parameters of the transition were swept individually to find their effects on the impedance matching. Then the design was refined by utilizing the information learned from these sweeps. Final adjustments of the dimensions were then performed by a few simulation steps to arrive at the dimensions that provide perfect impedance matching. The Bloch impedance is calculated as in [24] from the ABCD matrix of one unit-cell. The ABCD of the unit-cell is in turn found from the 15th root of the ABCD matrix of a 15-cell driven-mode simulation.

A fabricated sample of the DLWA is shown in Fig. 12(b). The fabricated DLWA is based on the parameters of a Rogers RO4003 board with dielectric constant $\varepsilon_r = 3.65$, and $\tan\delta = 0.0027$. To have minimum dielectric losses, a thin substrate with a height of 0.508 mm was utilized. Thickness and conductivity of copper-cladding are 18μm and 38.66 × 106 S/m respectively. The unit cell spacing is 10.82 mm. All rectangular perforations in the top and bottom metal of the guide are slots with dimensions 0.8 × 6 mm. Similar dimension slots are used for this target to realize the Q-balancing condition. The center-to-center separation of the vias for the SIW line

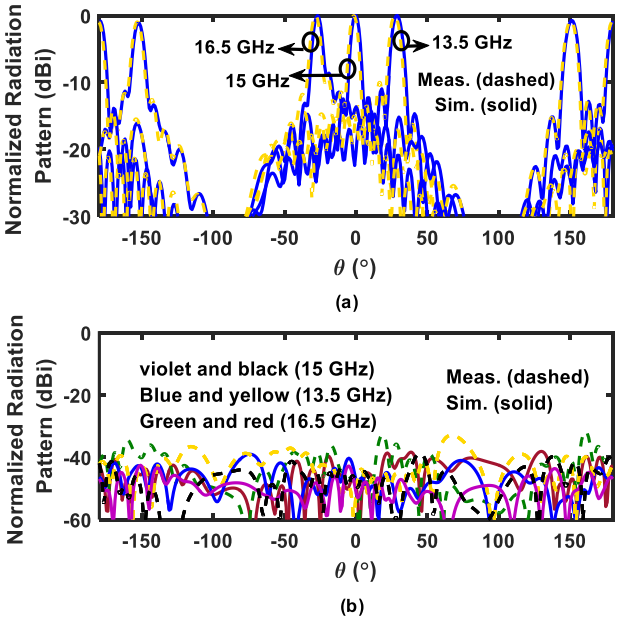

FIGURE 15. Changing the beam direction of the DLWA from backward to forward direction at $\varphi = 0$ plane. (a) co- polarization. (b) cross-polarization.

TABLE 1. Performance of the proposed DLWA.

Frequency (GHz)	Peak Gain (dB)	Beam Angle (°)	Total Efficiency (%)	Material Losses (%)
13.5	13.6	30	75	9
14	13.4	19	78	8
14.5	12.51	10	82	7
15	12	0	87	5
15.5	12	-10	90	5
16	11.9	-19	93	3
16.5	11.5	-30	90	1

and metallic column are 1.3525 mm and 1 mm, respectively. Also, the radius of all vias is 0.3 mm. The distance between the longitudinal slots from the vias of the SIW line is 0.4 mm and the distance between the transversal slots from the vias of the metallic column is 0.3 mm. The width of the microstrip line at the ports, the length and width of the transition are 1.116 mm, 3.3 mm and 11 mm, respectively. The width of the waveguide (center-to-center of vias of SIW line) is 12.3 mm.

The simulated and measured S-parameter of the DLWA for our prototype over a wide bandwidth around the design frequency of 15 GHz are shown in Fig. 13. Remarkable performance is obtained in the context of available LWA literature. It can be observed that the antenna is well matched ($|S_{11}| < -10$ dB) for all the bandwidth of 13.5 GHz to 16.5 GHz (20% fractional bandwidth.), i.e., all of the incident power is accepted. The $|S_{21}|$ shows that a very small fraction of the accepted power remains unused at the end of the DLWA. This power can be made to radiate with a longer antenna if needed. A frequency shift of around 0.1 GHz can be seen between design and fabrication. This difference is acceptable and is a result of the tolerances in the low-budget and medium quality local fabrication facility used by the authors. This in turn shows the viability of this design, without the need for very advanced fabrication facilities.

TABLE 2. Comparison between this work and prior art.

Ref.	Antenna Type	Technology Type	Unit Cells	Unit cell Length	Scanning Range with 10% Gain Variation (°)	$\|S_{11}\| < -10$ dB bandwidth (GHz)	Peak Gain (dB)	Cross Pol. (dB)	Radiation Efficiency (%)
[19]	Metamaterial	SIW	12	$0.22\lambda_0$ at 25.5 GHz	-17° to +13°	24 - 27 (11.8%)	13.2	-15	N/A
[20]	CRLH	Half-mode SIW	8	$0.6\lambda_0$ at 15 GHz	-15° to +20°	12.5 – 17.5 (33.3%)	15	-20	N/A
[21]	CRLH	Microstrip	20	$0.11\lambda_0$ at 4.4 GHz	-25° to +30°	3.9 – 4.9 (22.7%)	10.5	-25	70
[5]	DLWA	Metal WG	19	$0.41\lambda_0$ at 9.89 THz	-40° to +60°	8300 - 11100 (28%)	15	-40	92
[7]	DLWA	SIW	25	$0.47\lambda_0$ at 28 GHz	-20° to +25°	23.5 – 33 (33%)	16	-40	77
This work	DLWA	SIW	15	$0.54\lambda_0$ at 15 GHz	-30° to +30°	13.5 – 16.5 (20%)	12.5	-40	87

The simulated broadside radiation pattern for the 3D gain plot of the SIW DLWAs are shown in Fig. 14, demonstrating a directive beam exactly at broadside. These indicate that the DLWA does not exhibit a stopband at broadside, contrary to typical LWAs and confirm the dispersion diagram that was shown in Fig. 10. A gain of 12 dB can be seen for the proposed design. The continuous scanning ability of DLWA is depicted in Fig. 15(a) in the $\varphi = 0$ plane. As can be seen, this DLWA has a low sidelobe level with less than 1 dB gain variation throughout the frequency range from 13.5 GHz to 16.5 GHz. Also, The DLWA has a wide scan range from $-30°$ to $35°$. Fig. 15(b) shows the cross-polarization level of the proposed DLWA. As can be seen, a cross-polarization level of less than -40 dB is achieved in all of the frequency band.

The proposed DLWA radiates about 87% of the incident power around the broadside frequency which is generally essential in LWA literature. This can be seen in Fig. 16, which is the plot of the quantity $\mu_t = [1 - |S_{11}|^2 - |S_{21}|^2]\mu_r$, where μ_r is the simulated radiation efficiency. The leakage constant was designed to radiate most of the accepted power with reasonable length. As mentioned above, higher and lower leakage constants (by adjustment of slots) are also possible. The longer antenna ($N = 21$) provides a higher level of radiated power as also shown in Fig. 15 (due to the portion of the accepted power remainder at the end of the DLWA). Also, little part of the accepted power (about 5%) is lost in the structure due to metal and dielectric losses (equal to $[(1 - |S_{11}|^2 - |S_{21}|^2)/(1 - |S_{11}|^2) - \mu_r]$).

The performance of the proposed DLWA is given in Table 1. As can be seen, approximately all the gain values are almost the same without any gain reduction at the broadside frequency. The total efficiency and material losses are also reported, indicating that little fraction of the accepted power is lost (metal and dielectric losses). This table confirms that the proposed DLWA can provide beam steering by changing the frequency, without any detriment to any of the LWA performance metrics or gaps in radiation, through and around broadside.

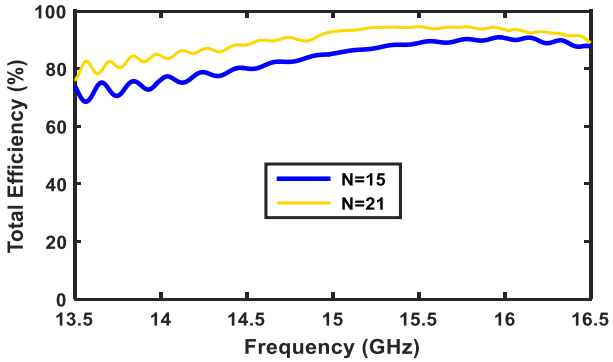

FIGURE 16. Simulated radiation efficiencies of DLWA.

Some features of this work are compared with previous works in Table 2. We give the comparison of antenna type, technology type, the number of unit cells, the length of unit cell, beam-scanning angle with 10% gain variation around the broadside, peak gain, $|S_{11}| < -10$ dB bandwidth, cross-polarization levels, and radiation efficiency. From Table 2, among all the fabricated and measured designs, our proposed design has the highest radiation efficiency and the best symmetric scanning range without gain variation. This is achieved while w.r.t cross-polarization levels, which is one of the best results. Another benefit that can be pointed out is that this performance has been obtained from a smaller number of unit cells, and the fabrication does not require access to very costly, accurate and high quality fabs.

VI. CONCLUSION

In this paper, we show that a simple periodic waveguide structure (with unit-cell comprised of two dissimilar WGs) can be designed to have a Dirac type dispersion, and find its governing relations. We then analytically design a Dirac PC in the microwave frequency band and experimentally demonstrate Dirac dispersion and leaky wave radiation from the structure, leading to a simple and effective DLWA. The DLWA is realized in SIW technology, but without any extra machining or through-holes as needed in its predecessors. Modal analysis and radiation pattern/mechanisms of the

DWLA are thoroughly analyzed and antenna performance is investigated. Measured results show excellent agreement with the simulated results. This SIW based DLWA demonstrates interesting features such as high directive omnidirectional fan beam with frequency scanning and simple feeding network, and is arguably the simplest DLWA to make thus far. These DLWAs may be utilized in various applications at microwave frequencies, in particular, communication systems, automotive radar, high-resolution sensor applications, weather radars.

REFERENCES

[1] A. H. C. Neto, F. Guinea, N. M. R. Peres, K. S. Novoselov, and A. K. Geim, "The electronic properties of graphene," *Rev. Mod. Phys.*, vol. 81, no. 1, pp. 109–162, Jan. 2009.
[2] X. Huang, Y. Lai, Z. H. Hang, H. Zheng, and C. T. Chan, "Dirac cones induced by accidental degeneracy in photonic crystals and zerorefractive-index materials," *Nature Matter.*, vol. 10, pp. 582–586, Aug. 2011.
[3] I. Liberal and N. Engheta, "Near-zero refractive index photonics," *Nature Photon.*, vol. 11, pp. 149–158, Mar. 2017.
[4] S. Rezaee and M. Memarian, "Dirac leaky wave antennas," in *Proc. 5th Int. Conf. Millimeter-Wave Terahertz Technol. (MMWaTT)*, Tehran, Iran, Dec. 2018, pp. 1–5.
[5] M. Memarian and G. V. Eleftheriades, "Dirac leaky-wave antennas for continuous beam scanning from photonic crystals," *Nature Commun.*, vol. 6, no. 1, pp. 1–9, May 2015.
[6] S. Rezaee, M. Memarian, and G. V. Eleftheriades, "SIW based dirac leaky-wave antenna," in *Proc. IEEE Int. Symp. Antennas Propag. USNC/URSI Nat. Radio Sci. Meeting*, Boston, MA, USA, Jul. 2018, pp. 125–126.
[7] S. Rezaee, M. Memarian, and G. V. Eleftheriades, "Dirac leaky wave antenna for millimeter wave applications," *IET Microw., Antennas Propag.*, vol. 14, no. 9, pp. 874–883, Jul. 2020.
[8] D. R. Jackson and A. A. Oliner, *Modern Antenna Handbook*, C. A. Balanis, Ed. Hoboken, NJ, USA: Wiley, 2008.
[9] W. Menzel and A. Moebius, "Antenna concepts for millimeter-wave automotive radar sensors," *Proc. IEEE*, vol. 100, no. 7, pp. 2372–2379, Jul. 2012.
[10] E. Im, C. Wu, and S. L. Durden, "Cloud profiling radar for the CloudSat mission," in *IEEE Aerosp. Electron. Syst. Mag.*, vol. 20, no. 10, pp. 15–18, Oct. 2005.
[11] L. Liu, C. Caloz, and T. Itoh, "Dominant mode leaky-wave antenna with backfire-to-endfire scanning capability," *Electron. Lett.*, vol. 38, no. 23, pp. 1414–1416, Nov. 2002.
[12] S. Rezaee, M. Memarian, and G. V. Eleftheriades, "2D dirac leaky wave antenna with circular polarization for millimeter-wave applications," in *Proc. IEEE Int. Symp. Antennas Propag. North Amer. Radio Sci. Meeting*, Montreal, QC, Canada, Jul. 2020, pp. 607–608.
[13] A. H. Dorrah, M. Memarian, and G. V. Eleftheriades, "Modal analysis and closure of the bandgap in 2D transmission-line grids," in *IEEE MTT-S Int. Microw. Symp. Dig.*, San Francisco, CA, USA, May 2016, pp. 1–4.
[14] A. H. Dorrah and G. V. Eleftheriades, "Pencil-beam single-point-fed dirac leaky-wave antenna on a transmission-line grid," *IEEE Antennas Wireless Propag. Lett.*, vol. 16, pp. 545–548, 2017.
[15] A. H. Dorrah and G. V. Eleftheriades, "Two-dimensional center-fed transmission-line-grid antenna for highly efficient broadside radiation," *Phys. Rev. A, Gen. Phys.*, vol. 10, no. 2, Aug. 2018, Art. no. 024024.
[16] S. Rezaee and M. Memarian, "Analytical study of open-stopband suppression in leaky-wave antennas," *IEEE Antennas Wireless Propag. Lett.*, vol. 19, no. 2, pp. 363–367, Feb. 2020.
[17] S. Rezaee and M. Memarian, "RGW based leaky wave antenna for terahertz application," in *Proc. 28th Iranian Conf. Electr. Eng. (ICEE)*, Tabriz, Iran, Aug. 2020, pp. 1–5.
[18] S. Rezaee, M. Memarian, and M. Ahmadian, "Parallel-plates-based dirac leaky wave antennas," *IET Microw., Antennas Propag.*, vol. 15, no. 15, pp. 1877–1890, Dec. 2021.
[19] W. Cao, Z. N. Chen, W. Hong, B. Zhang, and A. Liu, "A beam scanning leaky-wave slot antenna with enhanced scanning angle range and flat gain characteristic using composite phase-shifting transmission line," *IEEE Trans. Antennas Propag.*, vol. 62, no. 11, pp. 5871–5875, Nov. 2014.
[20] A. Sarkar, M. Adhikary, A. Sharma, A. Biswas, M. J. Akhtar, and Z. R. Hu, "Composite right/left-handed based compact and high gain leaky-wave antenna using complementary spiral resonator on HMSIW for Ku band applications," *IET Microw., Antennas Propag.*, vol. 12, no. 8, pp. 1310–1315, Jun. 2018.
[21] G.-C. Wu, G.-M. Wang, H.-X. Peng, X.-J. Gao, and J.-G. Liang, "Design of leaky-wave antenna with wide beam-scanning angle and low cross-polarisation using novel miniaturised composite right/left-handed transmission line," *IET Microw., Antennas Propag.*, vol. 10, no. 7, pp. 777–783, May 2016.
[22] A. Sarkar and S. Lim, "60 GHz compact larger beam scanning range PCB leaky-wave antenna using HMSIW for millimeter-wave applications," *IEEE Trans. Antennas Propag.*, vol. 68, no. 8, pp. 5816–5826, Aug. 2020.
[23] M. Guglielmi and D. R. Jackson, "Broadside radiation from periodic leaky-wave antennas," *IEEE Trans. Antennas Propag.*, vol. 41, no. 1, pp. 31–37, Jan. 1993.
[24] D. Pozar, *Microwave Engineering*, 4th ed. Hoboken, NJ, USA: Wiley, 2012.
[25] M. Memarian and R. R. Mansour, "Quad-mode and dual-mode dielectric resonator filters," *IEEE Trans. Microw. Theory Techn.*, vol. 57, no. 12, pp. 3418–3426, Dec. 2009.
[26] C. Caloz and T. Itoh, "Array factor approach of leaky-wave antennas and application to 1-D/2-D composite right/left-handed (CRLH) structures," *IEEE Microw. Wireless Compon. Lett.*, vol. 14, no. 6, pp. 274–276, Jun. 2004.
[27] D. Deslandes, "Design equations for tapered microstrip-to-Substrate integrated waveguide transitions," in *IEEE MTT-S Int. Microw. Symp. Dig.*, May 2010, pp. 704–707.
[28] S. Otto, A. Rennings, K. Solbach, and C. Caloz, "Transmission line modeling and asymptotic formulas for periodic leaky-wave antennas scanning through broadside," *IEEE Trans. Antennas Propag.*, vol. 59, no. 10, pp. 3695–3709, Oct. 2011.

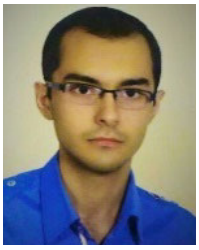

SINA REZAEE was born in Damghan, Iran, in 1994. He received the B.A.Sc. degree (Hons.) in electrical engineering from the Shahrood University of Technology, Shahrood, Iran, in 2016, and the M.Sc. degree from the Department of Electrical Engineering, Sharif University of Technology, in 2018.

His current research interests include electromagnetics, microwave engineering, antenna, RF circuit, and periodic structures.

Mr. Rezaee has received the IEEE AP/URSI 2018 Student Paper Competition Award.

MOHAMMAD MEMARIAN (Senior Member, IEEE) received the B.A.Sc. (Hons.) and M.A.Sc. degrees in electrical engineering from the University of Waterloo, Waterloo, ON, Canada, in 2007 and 2009, respectively, and the Ph.D. degree in electrical engineering from the University of Toronto, Toronto, ON, Canada, in 2015.

He was a Postdoctoral Fellow with the late Prof. Itoh at the University of California at Los Angeles, Los Angeles, CA, USA. He is currently an Assistant Professor with the Sharif University of Technology, Tehran, Iran. His current research interests include electromagnetics, antennas, metamaterials and metasurfaces, periodic structures, microwave filters and system components, and time-varying media.

Dr. Memarian is a member of the National Elites Foundation of Iran. He was a recipient of various awards, including the Nortel Networks Scholarship, the Natural Sciences and Engineering Research Council of Canada (NSERC), during his M.Sc., Ph.D., and postdoctoral research; the IEEE Antennas and Propagation Society Doctoral Research Award; the IEEE Microwave Theory and Techniques Society International Microwave Symposium (MTT-S IMS) Student Paper Competition Award, in 2009 and 2016 (and a finalist in 2017); the Best Oral Presentation Award of the IEEE MTT-S IMS, in 2009; and the IEEE AP/URSI 2018 Student Paper Competition Award.

GEORGE V. ELEFTHERIADES (Fellow, IEEE) received the M.S.E.E. and Ph.D. degrees in electrical engineering from the University of Michigan, Ann Arbor, MI, USA, in 1989 and 1993, respectively.

From 1994 to 1997, he was with the Swiss Federal Institute of Technology, Lausanne, Switzerland. He is currently a Professor with the Department of Electrical and Computer Engineering, University of Toronto, ON, Canada, where he is the Canada Research/Velma M. Rogers Graham Chair in nano- and micro-structured electromagnetic materials. He is a recognized international authority and pioneer in the area of metamaterials. These are man-made materials which have electromagnetic properties not found in nature. He introduced a method for synthesizing metamaterials using loaded transmission lines. Together with his graduate students, he provided the first experimental evidence of imaging beyond the diffraction limit and pioneered several novel antennas and microwave components using these transmission-line based metamaterials. His research has impacted the field by demonstrating the unique electromagnetic properties of metamaterials; used in lenses, antennas, and other microwave and optical components to drive innovation in fields, such as wireless and satellite communications, defence, medical imaging, microscopy, and automotive radar. He is also leading a group of graduate students and researchers in the areas of electromagnetic and optical metamaterials, and metasurfaces, antennas and components for broadband wireless communications, novel antenna beam-steering techniques, far-field super-resolution imaging, radars, plasmonic and nanoscale optical components, and fundamental electromagnetic theory.

Dr. Eleftheriades served as a member for the IEEE AP-Society Administrative Committee (AdCom), from 2007 to 2012, and was an IEEE AP-S Distinguished Lecturer, from 2004 to 2009. Articles that he coauthored have received numerous awards, such as the 2009 Best Paper Award from the IEEE Microwave and Wireless Propagation Letters, twice the R. W. P. King Best Paper Award from the IEEE Transactions on Antennas and Propagation (2008 and 2012), and the 2014 Piergiorgio Uslenghi Best Paper Award from the IEEE Antennas and Wireless Propagation Letters. He received the Ontario Premier's Research Excellence Award and the University of Toronto's Gordon Slemon Award, both in 2001. In 2004, he received an E.W.R. Steacie Fellowship from the Natural Sciences and Engineering Research Council of Canada. In 2009, he was elected as a fellow of the Royal Society of Canada and received the 2018 Research Leadership Award from the University of Toronto. He was a recipient of the 2008 IEEE Kiyo Tomiyasu Technical Field Award, the 2015 IEEE John Kraus Antenna Award, and the 2019 IEEE AP-S Distinguished Achievement Award. In 2018, he received the Research Leader Award from the Faculty of Applied Science and Engineering, University of Toronto. He served as the General Chair of the 2010 IEEE International Symposium on Antennas and Propagation, Toronto, ON, Canada. He also served as an Associate Editor for the IEEE Transactions on Antennas and Propagation.